Author Manuscript
Accepted for publication in a peer-reviewed journal

NIST National Institute of Standards and Technology • U.S. Department of Commerce

Published in final edited form as:
ACS Nano. 2016 October 25; 10(10): 9626–9636. doi:10.1021/acsnano.6b05127.

Characterization of Few-Layer 1T′ $MoTe_2$ by Polarization-Resolved Second Harmonic Generation and Raman Scattering

Ryan Beams[†], **Luiz Gustavo Cancado**[‡], **Sergiy Krylyuk**[†,||], **Irina Kalish**[†], **Berç Kalanyan**[†], **Arunima K. Singh**[†], **Kamal Choudhary**[†], **Alina Bruma**[†], **Patrick M. Vora**[§], **Francesca Tavazza**[†], **Albert V. Davydov**[†], and **Stephan J. Stranick**[†,*]

[†]Material Measurement Laboratory, National Institute of Standards and Technology, Gaithersburg, Maryland 20899, United States

[‡]Departamento de Física, Universidade Federal de Minas Gerais, Belo Horizonte, Minas Gerais 30123-970, Brazil

[||]Theiss Research, La Jolla, California 92037, United States

[§]Department of Physics and Astronomy, George Mason University, Fairfax, Virginia 22030, United States

Abstract

We study the crystal symmetry of few-layer 1T′ $MoTe_2$ using the polarization dependence of the second harmonic generation (SHG) and Raman scattering. Bulk 1T′ $MoTe_2$ is known to be inversion symmetric; however, we find that the inversion symmetry is broken for finite crystals with even numbers of layers, resulting in strong SHG comparable to other transition-metal dichalcogenides. Group theory analysis of the polarization dependence of the Raman signals allows for the definitive assignment of all the Raman modes in 1T′ $MoTe_2$ and clears up a discrepancy in the literature. The Raman results were also compared with density functional theory simulations and are in excellent agreement with the layer-dependent variations of the Raman modes. The experimental measurements also determine the relationship between the crystal axes and the polarization dependence of the SHG and Raman scattering, which now allows the anisotropy of polarized SHG or Raman signal to independently determine the crystal orientation.

Graphical Abstract

[*]Corresponding Author: stephan.stranick@nist.gov.

Notes
The authors declare no competing financial interest.

NOTE ADDED IN PROOF
During the review process ref 71 showed similar polarized Raman results for bulk 1T′ $MoTe_2$.

Supporting Information
The Supporting Information is available free of charge on the ACS Publications website at DOI: 10.1021/acsnano.6b05127.
Raman character tables, DFT details, substrate effects on the SHG signal, laser damage data, flake orientation information, white light contrast, additional SHG measurements, and the topographic images for Figure 4 (PDF)

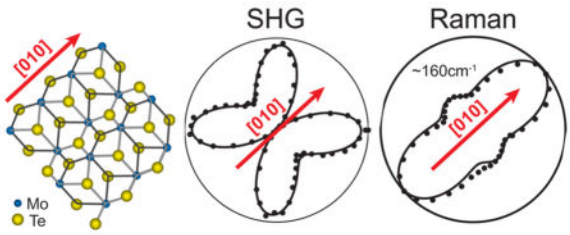

Keywords

two-dimensional material; Raman scattering; second harmonic generation; crystal symmetry; optical spectroscopy

The experimental realization of two-dimensional crystals has led to a new era of low-dimensional materials research. In conjunction with graphene and boron nitride, transition-metal dichalcogenides (TMDs) are actively being pursued for applications such as photovoltaics, flexible electronics, and chemical sensors.[1] While most of the research on TMDs has emphasized crystals with semiconducting behavior,[2] semimetallic TMDs have been shown to have large magnetoresistances[3] and superconductivity[4] as well as promising quantum spin Hall and Weyl semimetal properties.[5–8] One such example is molybdenum ditelluride ($MoTe_2$), which can be converted between semiconducting hexagonal phase (2H or α-$MoTe_2$) and semimetallic monoclinic phase (1T′ or β-$MoTe_2$) polymorphs. $MoTe_2$ exhibits large spin–orbit coupling and a near-infrared bandgap for 2H phase and strong magnetic properties for 1T′ phase.[9–11] Additionally at temperatures below ≈250 K, 1T′ converts to a semimetallic orthorhombic phase known as T_d[12–14] that shows promise as a Weyl semimetal,[8] which has been experimentally demonstrated in $MoTe_2$, WTe_2, $MoWTe_2$.[15–24] Studying the crystal phase 1T′ is relevant for a broader range of materials, such as ReS_2 and $ReSe_2$, which exhibit semiconductor properties with weak interlayer coupling.[25,26]

The unique properties of 1T′ $MoTe_2$ derive from the underlying crystal symmetry. Optical techniques, such as second harmonic generation (SHG)[27–33] and Raman scattering,[34–36] provide nondestructive means to probe the symmetries of two-dimensional materials. Due to the sensitivity of nonlinear optical processes to crystal symmetry, SHG allows for optical determination of the crystal orientation and symmetry of a crystal on a substrate. Since 1T′ is symmetric under inversion, no SHG is expected. However, as has been shown for other TMDs, the crystal symmetry can change for odd compared to even numbers of layers.[27–29] Similarly, the active Raman modes also depend on the crystal symmetry.[26,37–41] While the Raman properties of the 2H phase have been extensively studied,[10,42,43] the 1T′ phase has not been fully characterized, and there is significant discrepancy in the literature on the Raman modes assignment as well as the number of modes observed.[13,44–50]

We investigate the crystal symmetry of 1T′ $MoTe_2$ by measuring the polarization dependence of the SHG and Raman scattering. The bulk material is known to be monoclinic, belonging to the nonsymmorphic space group $P2_1/m$ (C_{2h}^2 in Schönflies notation, or #11 in the International Tables for Crystallography, Vol. A[51]).[12,52] However, the dependence of the

crystal symmetry on the number of layers (N) has not been studied for 1T′ $MoTe_2$. We find that the inversion symmetry is broken for even numbers of layers, leading to a strong SHG signal. The polarization dependence shows that samples with even layers are still monoclinic as expected for the 1T′ phase, but with symmetry defined by the symmorphic space group Pm (C_s^1, #6).[51] Similar behavior is expected for other crystals with 1T′ phase, such as ReS_2 and $ReSe_2$.[26] The wavelength and layer dependence of nonlinear susceptibility was measured, and the magnitude is comparable to other TMDs. We further characterized the optical properties of few-layer crystals with even and odd layers by assigning each Raman mode based on the polarization dependence. In addition, the imaginary parts of the complex components of the Raman tensors are required to explain the polarization dependence, which indicates that optical absorption in this material is significant. The polarization dependence also revealed that the totally symmetric Raman mode at ≈260 cm^{-1} is comprised of at least two peaks, although some simulations predict additional peaks.[44,49] These measurements help to clarify a discrepancy in the literature concerning the Raman scattering from 1T′ $MoTe_2$ as well as illustrate the changes in the crystal symmetry with layer parity. Finally, we demonstrate the relationship between the crystal axes and Raman polarization dependence, thereby enabling the identification of crystal orientation from Raman measurements alone.

RESULTS AND DISCUSSION

Bulk 1T′ $MoTe_2$ belongs to the C_{2h}^2 ($P2_1/m$, #11) non-symmorphic monoclinic space group.[12,52] The symmetry operations associated with this group are the identity E, a two-fold $C_{2y}(0,1/2,0)$ screw axis along the y direction (as defined in Figure 1a), a horizontal mirror σ_{xz}, and the inversion i. These symmetry elements are illustrated in Figure 1a, showing the top view of the crystal structure of monolayer 1T′ $MoTe_2$. The same symmetry operations hold for any sample with an odd number of layers, N, monolayer included. As such, they also belong to the C_{2h}^2 space group. However, the inversion symmetry is broken for 1T′ $MoTe_2$ with even layers, and the two-fold screw rotation is also no longer applicable. Since the reflection operation is still preserved, all samples with even layers fit into the C_s^1 (Pm, #6) space group. The breakdown of inversion symmetry for an even number of layers is seen from the side view of the crystal structure depicted in Figure 1b.

As discussed above, SHG is an excellent tool to characterize the presence or absence of inversion symmetry. Furthermore, crystal symmetry plays an important role in Raman spectroscopy. To study the symmetry properties of 1T′ $MoTe_2$ using these techniques, crystalline platelets were grown using an iodine-assisted chemical vapor transport (CVT) method and subsequently exfoliated onto an SiO_2/Si substrate. Figure 1c shows a light microscope image of the $MoTe_2$ sample with the various number of layers labeled, which were determined by atomic force microscopy (AFM). The direction (white dashed line) and rotation angle (θ) of the polarization relative to the x-axis are also indicated. The crystal axes, determined by electron backscatter diffraction (EBSD) and confirmed with SHG (Figure 1d), are also indicated. The phase and stoichiometry of the bulk material were confirmed with Raman spectroscopy, X-ray diffraction (XRD), X-ray photoelectron

spectroscopy (XPS), and high-angle annular dark-field scanning transmission electron microscopy (HAADF-STEM). While the exfoliation process removed the surface oxides, some oxides were detected using XPS in the unexfoliated regions of the bulk material. Figure 1e shows the HAADF-STEM image of the 1T′ $MoTe_2$ with the crystal diagram overlaid.

Topographic images acquired by an AFM of the $N = 3$, 4, and 12 regions of the sample are shown in Figures 2a,b, respectively. Thickness of the $N = 3$ and 4 regions was also confirmed using the relative amplitude of the strongest Raman peak (see Supporting Information). The SHG images of these two regions are shown in Figures 2c,d, respectively. The white lines in c and d represent the topographic outlines of the crystal (solid) and step edges (dashed). The SHG images were acquired using a 75 fs Ti:sapphire laser centered at 992 nm. The excitation wavelength was chosen to maximize the SHG signal and is nearly resonant with the electronic band structure at the Γ point.[48] While the signal may be stronger further into the infrared region, the wavelength was chosen to be at the far end of the Ti:sapphire gain curve. This image demonstrates that the trilayer ($N = 3$) and bulk (>25 layers) regions of the sample have no SHG signal. In contrast, the $N = 4$ region has a strong SHG signal, indicating broken inversion symmetry. In addition to the $N = 4$ region, a weaker SHG signal, by a factor 6, was observed from the $N = 12$ region in Figure 2d. The information contained in these images show that while bulk and $N = 3$ 1T′ $MoTe_2$ are symmetric under inversion (as expected for any 1T′ $MoTe_2$ sample with odd number of layers), the inversion symmetry is broken for even numbers of layers, as described in Figure 1.

To characterize the crystal symmetry and orientation of the sample, we measured the polarization dependence of the SHG signal. The SHG polarization dependence for the $N = 4$ region (black square in Figure 2c) and the $N = 12$ region (white circle in Figure 2d) with the excitation polarization and analyzer parallel (black) and crossed (red) are shown in Figure 2e,f, respectively. Each plot was normalized by the maximum signal from the parallel data set, and the zero angle is relative to the incident polarization (white arrow in Figure 2b). There are several important contrasts to materials with a 2H phase TMDs that have previously been measured. First, the signal is significantly stronger when the polarizer and analyzer are parallel. This means that the orientation of the crystal with respect to the excitation polarization is critical to maximize the SHG intensity even in the absence of an analyzer, unlike 2H materials where the summed parallel and crossed SHG signal intensity is independent of excitation polarization.[27–29] Second, the parity of the layer dependence is opposite of 2H materials, which are noninversion symmetric for monolayer and bulk.

Figures 3 and 4 show measurements from additional flakes to further explore the layer dependence of the SHG signal. Figure 3a,b shows the topography and SHG images with the AFM cross sections shown in the inset. The polarization dependence of the $N = 4$ and 6 regions with the excitation polarization and analyzer parallel (black) and crossed (red) are shown in Figure 3c,d, respectively. As in Figure 2, each plot was normalized by the maximum signal from the parallel data set, and the zero angle is relative to the incident polarization (white arrow in Figure 3b). The correlation between the topography and the SHG image as well as the similarity in the polarization dependence with the results shown in

Figure 2 provide additional evidence for layer-dependent inversion symmetry breaking. Figures 4a,b show white light images of additional larger crystals with the corresponding SHG images shown in Figures 4c,d. The insets show AFM linecuts along the black and blue dashed lines. In Figure 4c, the absence of any SHG signal combined with the bright 6L region provide an excellent illustration of the layer-dependent symmetry breaking. The polarization dependences of the 6L (black square) and 3L (red circle) regions were acquired in the parallel configuration and are shown in Figure 4e in black and red, respectively. These measurements determine the crystal orientation and verify the absence of SHG from the 3L region for all polarization directions. Figure 4f shows the polarization dependence acquired at three different locations in Figure 4d and an additional region in close proximity (see Supporting Information). The polarization dependence shows that the crystal orientation is the same for all regions. It is important to note that the polarization map shows that the SHG signals from the two 6L regions have similar maximum intensities despite the smaller sample (blue triangle) being brighter in Figure 4d. This intensity difference is due to the alignment of the excitation polarization with the crystal axis. Therefore, SHG intensity images cannot be used to estimate crystal thickness without aligning the incident polarization to the crystal axis. It is also important to note the change in the shape of the polarization maps for the different regions. While in the parallel configuration all the samples have a defined two-lobe pattern and zero signal along the zigzag direction, the shape varies from circular to a butterfly pattern. The butterfly pattern appears on smaller flakes and is likely caused by strain effects from the substrate or the influence of the edges. Both patterns are consistent with a C_s crystal as will be discussed.

The polarization dependence of the SHG signal extracted from regions with even layers is understood by considering the nonlinear properties of the C_s point group. The incident electric field, $\hat{e}_\omega{}^2 = [E_x{}^2\ E_y{}^2\ E_z{}^2\ 2E_yE_z\ 2E_xE_z\ 2E_xE_y] = [\cos^2\theta\ \sin^2\theta 0\ 0\ 0\ 2\cos\theta\ \sin\theta]$, generates a second harmonic signal along the $\hat{e}_{2\omega} = [\cos\theta\ \sin\theta\ 0]$ and $\hat{e}_{2\omega} = [-\sin\theta\ \cos\theta\ 0]$ directions for parallel and crossed polarizations, respectively. The intensity of the SHG signal, I_{SHG} can be expressed as

$$I_{\mathrm{SHG}} = |\hat{e}_{2\omega} \cdot \overleftrightarrow{\mathbf{d}} \hat{e}_\omega{}^2|^2 \quad (1)$$

where $\mathbf{d}\leftrightarrow$ is the second-order susceptibility tensor, $\chi^{(2)}$, in contracted notation.[53] For the C_s point group

$$\overleftrightarrow{\mathbf{d}} = \begin{pmatrix} d_{11} & d_{12} & d_{13} & 0 & d_{15} & 0 \\ 0 & 0 & 0 & d_{24} & 0 & d_{26} \\ d_{31} & d_{32} & d_{33} & 0 & d_{35} & 0 \end{pmatrix} \quad (2)$$

Substituting eq 2 into eq 1 leads to

$$I_{C_s}^{\parallel} = |\, d_{11}\cos^3\theta + (d_{12} + 2d_{26})\cos\theta\sin^2\theta \,|^2 \quad (3)$$

$$I_{C_s}^{\perp} = |\, d_{12}\sin^3\theta + (d_{11} - 2d_{26})\cos^2\theta\sin\theta \,|^2 \quad (4)$$

where $I_{C_s}^{\parallel}$ and $I_{C_s}^{\perp}$ are the parallel and crossed polarized signals, respectively (see Methods section). Eqs 3 and 4 are used to fit the SHG polarization dependence (solid lines in Figures 2e,f, 3c,d, and 4e,f) and confirm that even-layer 1T′ $MoTe_2$ belongs to the C_s point group. Unlike 2H materials, the various tensor elements do not have to be equal. According to eq 3, the SHG signal is minimized along the zigzag direction (*y*-axis in Figure 1) for the parallel polarization configuration, which is −43.2° and −42.4° in Figure 2c,d, respectively, as shown in Figure 1d. This slight difference in crystal axis is not surprising given that the two sample regions are not connected. For Figure 3, the SHG polar maps give a crystal orientation for the zigzag direction of −41.4° and −47.1° for the $N = 4$ and 6 regions, respectively, relative to the input polarization. In Figure 4e,f, the crystal orientations are −36.3° and −41.1° with respect to horizontal incident polarization, respectively.

These equations also help to explain the variations in the polarization maps. For example, due to the negative sign in the cross-polarized configuration, slight variations in tensor elements strongly affect the cross-polarized signal, as seen comparing the cross-polarized data between the $N = 4$ and 12 regions. In addition these equations explain the change between the two-lobe circular and butterfly polarization patterns. The polarization pattern is butterfly shaped when $d_{11} \leq d_{26}$ and a two-lobe circular pattern when $d_{11} > d_{26}$. Averaging the normalized coeffcients from the polarization maps in Figures 2 and 3 gives $d_{11} = 0.65$, $d_{12} = 0.5$, and $d_{26} = 0.78$, while averaging the circular patterns in Figure 4 gives $d_{11} = 0.96$, $d_{12} = 0.44$, and $d_{26} = 0.36$. Note that d_{12} remains approximately constant. The change in the polarization pattern can be thought of as a change in d_{26}, which originates from an incident field along the *x* and *y* axes, such as at 45°, and the SHG signal is along the *y* axis. While these two patterns do not correlate with the thickness of the crystal, smaller crystals do exhibit the butterfly pattern, which suggests that d_{26} is sensitive to strain from the substrate or edge effects. Based on these measurements, the polarization-dependent SHG signal provides a straightforward optical method for determining the crystallographic orientation for 1T′ $MoTe_2$.

The surface second-order susceptibility, d_s, of 1T′ $MoTe_2$ can be quantified by measuring reference samples under the same conditions. In this case, we measured monolayer MoS_2 prepared on the same substrate (see Supporting Information) and a 100 nm thick beta-barium borate (BBO) crystal. Using the wavelength dependence of d_s for MoS_2[28] gives a surface second-order susceptibility of $d_s = 1.0 \times 10^5$ pm^2/V at 992 nm for the $N = 4$ region in Figure 2. As a comparison, we also calibrated d_s of $MoTe_2$ using a 100 nm thick BBO crystal. Relative to the bulk crystal, d_s can be expressed as[27]

$$d_s = \frac{\lambda}{2\pi}\frac{1}{[n(\omega)+n(2\omega)]}\sqrt{\frac{I_s}{I_{BBO}}}d_{22} \quad (5)$$

where I_s and I_{BBO} are the surface and reference BBO SHG intensities, respectively, and $n(\omega)$ and $n(2\omega)$ are the refractive indices of the reference material at the fundamental and second harmonic frequencies, respectively. This approach leads to $d_s = 9 \times 10^4$ pm^2/V for the 4L region, which is in good agreement with the calibration using monolayer MoS_2. Since the excitation wavelengths used are far off the resonance for BBO, the wavelength dependence of d_{22} for BBO can be calculated using the Miller rule,[53] which indicates that d_{22} for BBO is nearly wavelength independent since the refractive index is approximately constant. While our samples were prepared on SiO_2/Si, the cavity effect from this substrate has been shown to result in a small correction to the SHG signal.[30,54] The impact of this effect was also verified by comparing SHG measurements of monolayer MoS_2 on a glass and an Si/SiO_2 substrate (see Supporting Information). Figure 5a shows the wavelength dependence of d_s for 1T′ $MoTe_2$ (blue circles) and monolayer MoS_2 (black squares). The MoS_2 measurements are in excellent agreement with refs 27 and 28, which provides support for our d_s 1T′ $MoTe_2$ values. It is important to note that the d_s values reported in refs 29, 30, and 32 are an order of magnitude larger compared to refs 27 and 28 because different calibration procedures were used. Unlike the resonance for MoS_2, 1T′ $MoTe_2$ shows d_s increases as the excitation wavelength increases as expected given the electronic states at ≈1 eV at the Γ point.[48] The absolute tensor elements, d_{ij}^{abs}, of 1T′ $MoTe_2$ are obtained using $d_{ij}^{abs} = d_s d_{ij}$, where d_{ij} is the normalized value discussed earlier. The layer dependence of d_s is shown in Figure 5b. The data were empirically fit using $d_s(N) = 1.8 \times 10^6$ N^{-2} pm^2/V. Our measurements show that the peak d_s for 1T′ $MoTe_2$ is of the same order of magnitude as MoS_2.

The crystal symmetry also determines the vibrational modes that are Raman active. Correctly assigning the Raman modes is particularly important for 1T′ $MoTe_2$, because there is a large amount of discrepancy in the literature on symmetry and the number of modes.[13,44–50] While density functional theory (DFT) has been used to attempt to assign the modes, the large number of active modes makes this task challenging, and the published results are inconsistent.[44,45,50] As discussed above, the 1T′ $MoTe_2$ with odd and even layers belong to the C_{2h}^2 and C_s^1 space groups, respectively. The Raman character tables are listed in the Supporting Information. Table 1 summarizes the symmetry of the vibrational modes for C_{2h}^2 and C_s^1 space groups. From group theory analysis, we expect $6N$ Raman modes with A_g symmetry and $3N$ Raman modes with B_g symmetry for 1T′ $MoTe_2$ with odd layers. For even layers, there should be $6N$ Raman modes with A′ and $3N$ Raman modes with A″ symmetry. In both cases (even and odd layers), $9N$ Raman modes are expected. While the symmetry change for even and odd numbers of layers drastically affects the SHG signal, the point groups C_{2h} and C_s have the same Raman tensors, and no significant changes are expected in the Raman spectra. This means that, for any value of N, we should observe 9

Raman modes, each one with *N*-degeneracy. Experimentally, these Raman modes can be assigned by measuring the polarization dependence of the Raman signal.

Figure 6 a,b shows the polarization dependence of Raman scattering for the $N = 12$ region in Figure 1 d for parallel and crossed polarized configurations, respectively. The data were acquired in a backscattering geometry using a 532 nm laser that was focused onto the sample using a 0.75 NA objective with the laser power at 350 μW. For higher laser powers, we observed long exposure laser damage on thicker regions ($N > 10$). However, at this laser power, we still observed laser-induced damage for the $N = 3$ and 4 regions, but it does not impact the presented results (Supporting Information). The polarization measurements allowed for all the modes in 1T′ $MoTe_2$ to be assigned, as indicated. These measurements resolve the discrepancy in the literature in identifying these modes and definitively assign the modes at ≈163 and ≈190 cm^{-1} as A_g and B_g, respectively. Our assignments agree with the ones presented in ref 50.

Raman spectra, without a polarization analyzer, of several regions in Figure 1c with different number of layers are shown in Figure 6c. Despite the changes in the symmetry type, the Raman spectra are similar throughout as expected. However, we observe several spectral differences for thinner regions of the sample. The Raman modes are wider for the $N = 4$ region, which is likely due to tellurium evaporation.[55,56] In addition, the higher energy mode in the doublet at ≈260 cm^{-1} blue shifts, which was previously observed.[44] The spectral separation for the doublet at ≈107 and ≈111 cm^{-1} increases, and the mode at ≈78 cm^{-1} blue shifts. These shifts are likely due to differences in the interlayer interactions of the various modes. Figure 6d shows two example spectra for the $N = 4$ and 12 regions in a parallel configuration and shows that the peak at ≈260 cm^{-1} is a doublet. Notably these two modes are both totally symmetric (A' for even layers, and A_g for odd layers), but are out of phase, as shown in polarization maps (Figure 6 a,b). While other works have shown this doublet, the polarization dependence has not been previously characterized.[13,14,50]

To gain a more detailed understanding of the Raman behavior of 1T′ $MoTe_2$, the polarization dependence needs to be fit using the Raman tensors. Using the coordinate system defined in Figure 1, the Raman tensors are

$$\overleftrightarrow{\mathbf{R}}_{A_g} = \overleftrightarrow{\mathbf{R}}_{A'} = \begin{pmatrix} a & 0 & d \\ 0 & b & 0 \\ d & 0 & c \end{pmatrix} \quad (6)$$

$$\overleftrightarrow{\mathbf{R}}_{B_g} = \overleftrightarrow{\mathbf{R}}_{A''} = \begin{pmatrix} 0 & f & 0 \\ f & 0 & g \\ 0 & g & 0 \end{pmatrix} \quad (7)$$

Often the components of the Raman tensors are treated as real values, because the imaginary part of the Raman susceptibility is negligible for transparent materials. However, for

materials with significant absorption, the components can be complex as was recently shown for black phosphorus and WTe_2.[57,58] In this case, tensor elements are defined as $R_{ij} = |R_{ij}| e^{i\phi R_{ij}}$. Similar to the SHG analysis, the Raman signal is calculated using $S = |\hat{e}_s \cdot \mathbf{R} \leftrightarrow \hat{e}_i|^2$, where the incident beam is $\hat{e}_i = [\cos\theta \sin\theta 0]$ and the scattered field is expressed as $\hat{e}_s = [\cos\theta \sin\theta 0]$ and $\hat{e}_s = [-\sin\theta \cos\theta 0]$ for parallel and cross-polarizations, respectively. Combining these expressions with eqs 6 and 7 leads to

$$S^{\parallel}_{A_g} = S^{\parallel}_{A'} = |a|^2\cos^4\theta + |b|^2\sin^4\theta + \frac{|a||b|}{2}\cos\phi_{ab}\sin^2 2\theta \quad (8)$$

$$S^{\perp}_{A_g} = S^{\perp}_{A'} = \frac{1}{4}(|a|^2 + |b|^2 - 2|a||b|\cos\phi_{ab})\sin^2 2\theta \quad (9)$$

$$S^{\parallel}_{B_g} = S^{\parallel}_{A''} = |f|^2\sin^2 2\theta \quad (10)$$

$$S^{\perp}_{B_g} = S^{\perp}_{A''} = |f|^2\cos^2 2\theta \quad (11)$$

for the parallel and crossed polarized Raman signal for the two modes (see Methods section). ϕ_{ab} is the complex phase, and in the case of a real valued Raman tensor $\phi_{ab} = 0$. Notice that the complex phase cancels for the B_g and A'' modes.

The Raman spectra in Figures 6a,b were fit using Lorentzians, and the resulting amplitudes are plotted in Figure 7. The polarization dependence for the parallel (black) and crossed (red) polarized configurations was normalized by the maximum amplitude from the parallel configuration. Figure 7 plots 10 modes, where the first 9 are the modes pointed out in Figure 6. The last peak was used to fit the high-energy shoulder on the peak at ≈260 cm^{-1}, which means for the $N = 12$ sample, the peaks from 250 to 260 cm^{-1} were treated as a triplet. This was not necessary for the $N = 4$ and 3 regions, which could indicate that there is an additional peak for thicker samples. The polarization dependence of the amplitudes was subsequently fit with eqs 8–11, shown as solid lines in Figure 7. While the real valued tensor overall fits the data, there are significant deviations, such as the secondary peaks and strong crossed polarized signal shown in Figure 7d and to a lesser extent in Figures 7f,i,j. This behavior shows that there is significant absorption in 1T′ $MoTe_2$ and the complex nature of the Raman susceptibility is important. While this is an unusual behavior for transparent crystals, it is not altogether surprising given the metallic nature of 1T′ $MoTe_2$. The polarization measurements also show that all the A_g (A′) modes are maximized for incident polarization along the zigzag direction (y axis), except the A_g (A′) mode at ≈260 cm^{-1}. Similar plots for the $N = 4$ and 3 regions in Figure 1d are shown in Figures 8a,b,

respectively. The peak shifts between the $N = 4$ and 3 regions agree with the trends shown in Figures 6c,d. The fits for the peak at ≈94 cm^{-1} were omitted due to the low signal level. These polarization measurements directly demonstrate that the symmetry change from C_{2h}^2 ($N = 3$) to C_s^1 ($N = 4$) does not change the symmetry of the Raman modes. Additional Raman measurements from the sample in Figure 3 are in the Supporting Information. The Raman modes for the $N = 12$ region are summarized in Figure 9, and the red or blue shift with the number of layers is indicated.

In agreement with the experiments, DFT simulations of N-layer ($N = 1$–4 and ∞) 1T′ $MoTe_2$ show that Raman spectra are similar despite the change in symmetry between odd and even number of layers, as shown in Figure 10. The DFT computed results also show that the N-layer 1T′ $MoTe_2$ has a characteristic blue shift in the higher energy modes (around ≈ 260 cm^{-1}) and a spectral separation of the B_g and A_g modes at ≈105 and ≈110 cm^{-1}, respectively, as the number of layers decreases. Figure 10 shows that the blue shift in the higher energy modes is apparent when a comparison is made between 1-layer and bulk structure. In the 3-layer and 4-layer 1T′ $MoTe_2$, the majority of the higher energy modes follow the same trend. A few outlying modes toward higher frequencies are predicted by our DFT calculations, which could either be the experimentally observed peak shoulders or modes with low Raman intensities. Note that the simulated normal-mode frequencies agree extremely well with the experimentally measured frequencies; for instance, the peak doublet at 259 cm^{-1} is computed to be within 3% of the experimentally measured value, see Figure 9.

CONCLUSION

We have measured the polarization dependence of the SHG and Raman signal, from 1T′ $MoTe_2$. These measurements experimentally demonstrate the layer parity dependence of the inversion symmetry of 1T′ $MoTe_2$ and resolve the discrepancy in the literature on the assignment of the Raman modes. The SHG analysis shows symmetry changing from odd (non-symmorphic monoclinic space group C_{2h}^2) to even (symmorphic monoclinic space group C_s^1) numbers of layers. The breakdown in the inversion symmetry for even numbers of layers allows for the crystal symmetry and orientation to be determined by means of polarization-dependent SHG measurements. Furthermore, the crystal orientation can also be independently determined using the anisotropic polarized Raman response. Despite the difference in the crystal symmetry for even and odd numbers of layers, all Raman modes can be explained by only two symmetry types. Finally, the 1T′ phase is known to be a precursor to the T_d phase in $MoTe_2$, which shows promise as a Weyl semimetal, and thus SHG will also be an excellent tool for probing this transition.

METHODS

1T′ $MoTe_2$ Growth

$MoTe_2$ crystals were produced using CVT with iodine as the transport agent. $MoTe_2$ powder was synthesized by annealing molybdenum (99.999%) and tellurium (99.9%) powders

mixed in a stoichiometric proportion at 750 °C for 72 h in an evacuated and sealed quartz ampule. Single crystals of $MoTe_2$ were created by sealing approximately 2 g of polycrystalline $MoTe_2$ powder and a small amount of iodine (99.8%, 4 mg/cm^3) in evacuated 17 cm long quartz ampules. The ampules were placed in a furnace with a temperature gradient such that the $MoTe_2$ charge was kept at 1000 °C and temperature at the opposite end of the ampule was about 950 °C. Finally the ampule was quenched in ice water after 7 days of growth to retain the 1T′ phase.

X-ray Diffraction

According to the θ–2θ XRD scans, single crystals produced by the post-quenching method have crystallized in the 1T′ structure (point group C_{2h}) with strong (0001) texture. The lattice parameters $a = 6.339(3)$Å, $b = 3.466(4)$Å, $c = 13.844(3)$Å, and $\beta = 93.84(5)°$ were obtained by the cell refinement method using MDI-JADE 6.5 software (Jade 6.5, Materials Data, Inc. Livermore, CA., 2015).[59]

X-ray Photoelectron Spectroscopy

XPS was carried out using a monochromated Al Kα source operated at 104 W and a hemispherical analyzer. Spectra were acquired at an analyzer pass energy of 10 eV, and the analysis area was approximately 0.1 mm × 0.1 mm. Spectra were calibrated against C 1s (C–H, 284.8 eV) assigned to adventitious carbon.

$MoTe_2$ crystalline platelets were mounted on carbon tape and exfoliated immediately prior to loading into the vacuum chamber. The atomic composition of the surface was 29.3 ± 5.1% C, 22.0 ± 1.9% Mo, 3.2 ± 1.8% O, and 45.6 ± 3.4% Te. Errors reported are estimates of uncertainties associated with peak fitting and were calculated using a Monte Carlo analysis implemented in the CasaXPS software. One doublet in the Te region corresponding to $3d_{5/2}$ and $3d_{3/2}$ spin–orbit peaks was found at 572.5 and 582.9 eV ($\Delta = 10.4$ eV). Mo $3d_{5/2}$ and $3d_{3/2}$ components were found at 227.9 and 231.1 eV ($\Delta = 3.2$ eV). Peaks associated with TeO_2 were notably absent in the Te 3p and 3d spectra, but a small shoulder in the Mo 3d region ascribed to MoO_x was detectable. A small quantity of Te or Mo suboxide cannot be excluded based on the amount of oxygen measured on the surface.

Electron Backscatter Diffraction

Morphology of the samples was examined in a JEOL JSM-7100F field emission scanning electron microscope (FESEM). The identification of phases and crystallographic orientations of the flakes was performed by EBSD using an Oxford Instruments HKL Nordlys EBSD detector and NanoAnalysis AZtec 3.1 software.

Scanning Transmission Electron Microscopy

HAADF-STEM images were recorded on an aberration-corrected FEI Titan 80–300 operated at 300 kV, using a camera length of 100 mrad corresponding to inner and outer collection angles of 70.6 and 399.5 mrad, respectively. The sample has been crushed in ethanol, and a drop of solution was placed on a 400-mesh TEM grid (Agar Inc.). Here, the observed HAADF-STEM intensity is proportional to the atomic number Z ($I \approx Z^{\alpha}$), where α is a proportionality factor between 1.5 and 2.[60] Given the di3erences between the atomic

number of Mo (Z_{Mo} = 42) and Te (Z_{Te} = 52), the intensity variations can be attributed to the presence of two elements in the observed single crystals.

Atomic Force Microscope

The topographic images were acquired on an atomic force microscope operating in tapping mode. A mechanically stiff (k = 42 N/m) cantilever with a large driving amplitude and set point was used to mitigate the effects of the tip–material interactions and maintain a repulsive interaction.[61] The thickness measurements were also compared to single layer graphene measurements, verified using Raman spectroscopy. To minimize oxidation, the samples were stored in a nitrogen environment between measurements.

Second Harmonic Generation and Raman Measurements

The Raman and SHG data were acquired by placing the sample on an x–y piezo scan stage. For the SHG measurements, the sample was excited by a femtosecond Ti:sapphire laser (≈75 fs, 80 MHz) centered at 992 nm using a microscope objective (0.75 NA). The average power was 0.6 mW at the sample. The sample was raster-scanned through the focus to build up images, and the resulting signal was collected using the same microscope objective and sent to either a single photon counting module with a narrow bandpass filter for rapid imaging or a spectrometer and a charge-coupled device (CCD). The Raman setup used 0.35 mW from a 532 nm laser using a microscope objective (0.75 NA). The spectra were acquired using a 500 mm focal length spectrometer with a 2400 lines/mm grating and CCD. Due to the low power levels, each spectral acquisition was 2 min. The spectra were calibrated using an Ar lamp, and the laser frequency was measured with a wavemeter. No signatures of MoO_2, MoO_3, or TeO_2 were measurable in the Raman spectra for the thicker samples. However, the small peak at ≈285 cm^{-1} in the N = 4 sample could be from amorphous MoO_3 given the spectral location and lack of polarization dependence.

The SHG and Raman polarization dependence was measured by sending the linearly polarized excitation beam through a motorized achromatic halfwave plate, and the signal was analyzed using a motorized linear polarizer. Finally, the analyzed signal was sent through a multimode fiber that scrambled the polarization prior to the spectrometer to remove the polarization dependence of grating. We verified the system using a polarimeter and by measuring the polarization dependence of monolayer molybdenum disulfide (MoS_2) on the SHG and Raman instruments. Figure 2 was generated by taking a 10 s spectrum at each position; the resulting signal was fit with a Gaussian of fixed position and width. Despite low-power levels for the Raman measurements, some laser damage was observed for very thin samples (see Supporting Information).

Raman Mode Simulations

All simulations were based on DFT using the projector-augmented wave method as implemented in the plane-wave code VASP.[62–65] All the simulations were performed using the vdW-DF-optB88 exchange–correlation functional.[66–68] A k-point mesh of at least 10 × 18 × 5 for the bulk 1T′-$MoTe_2$ and that of 10 × 18 × 1 for the N-layer (N = 1–4) 1T′-$MoTe_2$ with a 600 eV energy cutoff resulted in an accuracy of the total energies of 1 meV/unitcell. The $5s^2 5p^4$ and $4d^5 5s$ electrons were considered as the valence electrons for Te and Mo,

respectively. Including the semicore $4s^2p^6$ electrons for Mo had a negligible effect on the results, as, for instance, the lattice parameters of bulk 1T′-$MoTe_2$ changed by <0.1%. The *n*-layer $MoTe_2$ was simulated using a slab geometry with a vacuum spacing of 18 Å which ensures that the interactions between the periodic cells were negligible.

The bilayer, trilayer, and quad-layer of $MoTe_2$ were simulated in the same A-B stacking between the layers as in the bulk material. The structures were relaxed until the forces on the atoms were <1 meV/Å. The calculations of the phonon frequencies at the Gamma point were performed using DFT simulations (DFPT) on the primitive cells of the materials. All the measured peak positions of bulk 1T′-$MoTe_2$ were within 6% of the DFT computed values. Irreducible representation of normal modes was obtained from the PHONOPY program[69] and the Bilbao Crystallographic Server.[70]

Supplementary Material

Refer to Web version on PubMed Central for supplementary material.

Acknowledgments

R.B. acknowledges the NIST/National Research Council Research Associate Program (NRC RAP) for its support. P.M.V. acknowledges support from the GMU OSCAR Program. L.G.C. acknowledges the Brazilian agencies CNPq and FAPEMIG. A.B. acknowledges MGI. A.V.D., S.K., and I.K. acknowledge the support of Material Genome Initiative funding allocated to NIST. A.K.S. is funded by the Professional Research Experience Postdoctoral Fellowship under award no. 70NANB11H012. This research used computational resources provided by the Texas Advanced Computing Center under contract TG-DMR150006. This work used the Extreme Science and Engineering Discovery Environment (XSEDE), which was supported by National Science Foundation grant number ACI-1053575. We thank C. Janisch, I. Levin, J. Maslar, C. Michaels, and J. Ribeiro-Soares for fruitful discussions.

References

1. Geim AK, Grigorieva IV. Van der Waals Heterostructures. Nature. 2013; 499:419–425. [PubMed: 23887427]
2. Mak KF, Shan J. Photonics and Optoelectronics of 2D Semiconductor Transition Metal Dichalcogenides. Nat Photonics. 2016; 10:216–226.
3. Ali MN, Xiong J, Flynn S, Tao J, Gibson QD, Schoop LM, Liang T, Haldolaarachchige N, Hirschberger M, Ong NP, Cava RJ. Large, Non-Saturating Magnetoresistance in WTe_2. Nature. 2014; 514:205–208. [PubMed: 25219849]
4. Kang D, Zhou Y, Yi W, Yang C, Guo J, Shi Y, Zhang S, Wang Z, Zhang C, Jiang S, Li A, Yang K, Wu Q, Zhang G, Sun L, Zhao Z. Superconductivity Emerging from a Suppressed Large Magnetoresistant State in Tungsten Ditelluride. Nat Commun. 2015; 6:7804. [PubMed: 26203807]
5. Qian X, Liu J, Fu L, Li J. Quantum Spin Hall Effect in Two-Dimensional Transition Metal Dichalcogenides. Science. 2014; 346:1344–1347. [PubMed: 25504715]
6. Sun Y, Wu SC, Ali MN, Felser C, Yan B. Prediction of Weyl Semimetal in Orthorhombic $MoTe_2$. Phys Rev B: Condens Matter Mater Phys. 2015; 92:161107.
7. Soluyanov AA, Gresch D, Wang Z, Wu Q, Troyer M, Dai X, Bernevig BA. Type-II Weyl Semimetals. Nature. 2015; 527:495–498. [PubMed: 26607545]
8. Qi Y, Naumov PG, Ali MN, Rajamathi CR, Schnelle W, Barkalov O, Hanfland M, Wu SC, Shekhar C, Sun Y, Süß V, Schmidt M, Schwarz U, Pippel E, Werner P, Hillebrand R, Förster T, Kampert E, Parkin S, Cava RJ, et al. Superconductivity in Weyl Semimetal Candidate $MoTe_2$. Nat Commun. 2016; 7:11038. [PubMed: 26972450]
9. Vellinga M, De Jonge R, Haas C. Semiconductor to Metal Transition in $MoTe_2$. J Solid State Chem. 1970; 2:299–302.

10. Ruppert C, Aslan OB, Heinz TF. Optical Properties and Band Gap of Single-and Few-Layer $MoTe_2$ Crystals. Nano Lett. 2014; 14:6231–6236. [PubMed: 25302768]
11. Pradhan NR, Rhodes D, Feng S, Xin Y, Memaran S, Moon BH, Terrones H, Terrones M, Balicas L. Field-Effect Transistors Based on Few-Layered α-$MoTe_2$. ACS Nano. 2014; 8:5911–5920. [PubMed: 24878323]
12. Dawson W, Bullett D. Electronic Structure and Crystallography of $MoTe_2$ and WTe_2. J Phys C: Solid State Phys. 1987; 20:6159.
13. Chen S-Y, Goldstein T, Ramasubramaniam A, Yan J. Inversion-Symmetry-Breaking-Activated Shear Raman Bands in T′-$MoTe_2$. 2016
14. Joshi J, Stone I, Beams R, Krylyuk S, Kalish I, Davydov A, Vora P. Phonon Anharmonicity in Bulk T_d-$MoTe_2$. Appl Phys Lett. 2016; 109:031903.
15. Chang TR, Xu SY, Chang G, Lee CC, Huang SM, Wang B, Bian G, Zheng H, Sanchez DS, Belopolski I, Alidoust N, Neupane M, Bansil A, Jeng HT, Lin H, Hasan MZ. Prediction of an Arc-Tunable Weyl Fermion Metallic State in $Mo_xW_{1-x}Te_2$. Nat Commun. 2016; 7:10639. [PubMed: 26875819]
16. Xu N, Wang Z, Weber A, Magrez A, Bugnon P, Berger H, Matt C, Ma J, Fu B, Lv BQ, Plumb NC, Radovic M, Pomjakushina E, Conder K, Qian T, Dil JH, Mesot J, Ding H, Shi M. Discovery of Weyl Semimetal State Violating Lorentz Invariance in $MoTe_2$. 2016
17. Belopolski I, Xu SY, Ishida Y, Pan X, Yu P, Sanchez DS, Zheng H, Neupane M, Alidoust N, Chang G, et al. Fermi Arc Electronic Structure and Chern Numbers in the Type-II Weyl Semimetal Candidate $Mo_xW_{1-x}Te_2$. Phys Rev B: Condens Matter Mater Phys. 2016; 94:085127.
18. Wu Y, Jo NH, Mou D, Huang L, Bud'ko S, Canfield P, Kaminski A. Observation of Fermi Arcs in Type-II Weyl Semimetal Candidate WTe_2. 2016
19. Wang C, Zhang Y, Huang J, Nie S, Liu G, Liang A, Zhang Y, Shen B, Liu J, Hu C, Ding Y, Liu D, Hu Y, He S, Zhao L, Yu L, Hu J, Wei J, Mao Z, Shi Y, et al. Spectroscopic Evidence of Type II Weyl Semimetal State in WTe_2. 2016
20. Deng K, Wan G, Deng P, Zhang K, Ding S, Wang E, Yan M, Huang H, Zhang H, Xu Z, Denlinger J, Fedorov A, Yang H, Duan W, Yao H, Wu Y, Fan YS, Zhang H, Chen X, Zhou S. Experimental Observation of Topological Fermi Arcs in Type-II Weyl Semimetal $MoTe_2$. 2016
21. Liang A, Huang J, Nie S, Ding Y, Gao Q, Hu C, He S, Zhang Y, Wang C, Shen B, Liu J, Ai P, Yu L, Sun X, Zhao W, Lv S, Liu D, Li C, Zhang YY, Hu Y, et al. Electronic Evidence for Type II Weyl Semimetal State in $MoTe_2$. 2016
22. Jiang J, Liu Z, Sun Y, Yang H, Rajamathi R, Qi Y, Yang L, Chen C, Peng H, Hwang CC, Sun SZ, Mo SK, Vobornik I, Fujii J, Parkin SSP, Felser C, Yan BH, Chen YL. Observation of the Type-II Weyl Semimetal Phase in $MoTe_2$. 2016
23. Huang L, McCormick TM, Ochi M, Zhao Z, Suzuki M-t, Arita R, Wu Y, Mou D, Cao H, Yan J, Trivedi N, Kaminski A. Spectroscopic Evidence for Type II Weyl Semimetal State in $MoTe_2$. 2016
24. Tamai A, Wu Q, Cucchi I, Bruno F, Ricco S, Kim T, Hoesch M, Barreteau C, Giannini E, Bernard C, Soluyanov AA, Baumberger F. Fermi Arcs and Their Topological Character in the Candidate Type-II Weyl Semimetal $MoTe_2$. 2016
25. Tongay S, Sahin H, Ko C, Luce A, Fan W, Liu K, Zhou J, Huang YS, Ho CH, Yan J. Monolayer Behaviour in Bulk ReS_2 Due to Electronic and Vibrational Decoupling. Nat Commun. 2014; 5:3252. [PubMed: 24500082]
26. Lorchat E, Froehlicher G, Berciaud S. Splitting of Interlayer Shear Modes and Photon Energy Dependent Anisotropic Raman Response in N-Layer $ReSe_2$ and ReS_2. ACS Nano. 2016; 10:2752–2760. [PubMed: 26820232]
27. Li Y, Rao Y, Mak KF, You Y, Wang S, Dean CR, Heinz TF. Probing Symmetry Properties of Few-Layer MoS_2 and h-BN by Optical Second-Harmonic Generation. Nano Lett. 2013; 13:3329–3333. [PubMed: 23718906]
28. Malard LM, Alencar TV, Barboza APM, Mak KF, de Paula AM. Observation of Intense Second Harmonic Generation from MoS_2 Atomic Crystals. Phys Rev B: Condens Matter Mater Phys. 2013; 87:201401.
29. Kumar N, Najmaei S, Cui Q, Ceballos F, Ajayan PM, Lou J, Zhao H. Second Harmonic Microscopy of Monolayer MoS_2. Phys Rev B: Condens Matter Mater Phys. 2013; 87:161403.

30. Janisch C, Wang Y, Ma D, Mehta N, Elías AL, Perea-López N, Terrones M, Crespi V, Liu Z. Extraordinary Second Harmonic Generation in Tungsten Disulfide Monolayers. Sci Rep. 2014; 4:5530. [PubMed: 24984953]
31. Wang G, Marie X, Gerber I, Amand T, Lagarde D, Bouet L, Vidal M, Balocchi A, Urbaszek B. Giant Enhancement of the Optical Second-Harmonic Emission of WSe_2 Monolayers by Laser Excitation at Exciton Resonances. Phys Rev Lett. 2015; 114:097403. [PubMed: 25793850]
32. Ribeiro-Soares J, Janisch C, Liu Z, Elías A, Dresselhaus M, Terrones M, Cançado L, Jorio A. Second Harmonic Generation in WSe_2 2D. Mater. 2015; 2:045015.
33. David SN, Zhai Y, van der Zande AM, O'Brien K, Huang PY, Chenet DA, Hone JC, Zhang X, Yin X. Rapid, All-Optical Crystal Orientation Imaging of Two-Dimensional Transition Metal Dichalcogenide monolayers. Appl Phys Lett. 2015; 107:111902.
34. Ferrari AC, Basko DM. Raman Spectroscopy as a Versatile Tool for Studying the Properties of Graphene. Nat Nanotechnol. 2013; 8:235–246. [PubMed: 23552117]
35. Beams R, Cançado LG, Novotny L. Raman Characterization of Defects and Dopants in Graphene. J Phys : Condens Matter. 2015; 27:083002. [PubMed: 25634863]
36. Zhang X, Qiao XF, Shi W, Wu JB, Jiang DS, Tan PH. Phonon and Raman Scattering of Two-Dimensional Transition Metal Dichalcogenides from Monolayer, Multilayer to Bulk Material. Chem Soc Rev. 2015; 44:2757–2785. [PubMed: 25679474]
37. Luo X, Zhao Y, Zhang J, Toh M, Kloc C, Xiong Q, Quek SY. Effects of Lower Symmetry and Dimensionality on Raman Spectra in Two-Dimensional WSe_2. Phys Rev B: Condens Matter Mater Phys. 2013; 88:195313.
38. Ribeiro-Soares J, Almeida R, Barros E, Araujo P, Dresselhaus M, Cançado L, Jorio A. Group Theory Analysis of Phonons in Two-Dimensional Transition Metal Dichalcogenides. Phys Rev B: Condens Matter Mater Phys. 2014; 90:115438.
39. Ribeiro-Soares J, Almeida R, Cancado L, Dresselhaus M, Jorio A. Group Theory for Structural Analysis and Lattice Vibrations in Phosphorene Systems. Phys Rev B: Condens Matter Mater Phys. 2015; 91:205421.
40. Kolobov, AV, Tominaga, J. Two-Dimensional Transition-Metal Dichalcogenides. Springer International Publishing; Switzerland: 2016. 227–294.
41. Saito R, Tatsumi Y, Huang S, Ling X, Dresselhaus M. Raman Spectroscopy of Transition Metal Dichalcogenides. J Phys : Condens Matter. 2016; 28:353002. [PubMed: 27388703]
42. Yamamoto M, Wang ST, Ni M, Lin YF, Li SL, Aikawa S, Jian WB, Ueno K, Wakabayashi K, Tsukagoshi K. Strong Enhancement of Raman Scattering from a Bulk-Inactive Vibrational Mode in Few-Layer $MoTe_2$. ACS Nano. 2014; 8:3895–3903. [PubMed: 24654654]
43. Guo H, Yang T, Yamamoto M, Zhou L, Ishikawa R, Ueno K, Tsukagoshi K, Zhang Z, Dresselhaus MS, Saito R. Double Resonance Raman Modes in Monolayer and Few-Layer $MoTe_2$. Phys Rev B: Condens Matter Mater Phys. 2015; 91:205415.
44. Keum DH, Cho S, Kim JH, Choe DH, Sung HJ, Kan M, Kang H, Hwang JY, Kim SW, Yang H, Chang KJ, Lee YH. Bandgap Opening in Few-Layered Monoclinic $MoTe_2$. Nat Phys. 2015; 11:482–486.
45. Cho S, Kim S, Kim JH, Zhao J, Seok J, Keum DH, Baik J, Choe DH, Chang K, Suenaga K, Kim SW, Lee YH, Yang H. Phase Patterning for Ohmic Homojunction Contact in $MoTe_2$. Science. 2015; 349:625–628. [PubMed: 26250680]
46. Park JC, Yun SJ, Kim H, Park JH, Chae SH, An SJ, Kim JG, Kim SM, Kim KK, Lee YH. Phase-Engineered Synthesis of Centimeter-Scale 1T′-and 2H-Molybdenum Ditelluride Thin Films. ACS Nano. 2015; 9:6548–6554. [PubMed: 26042796]
47. Zhou L, Xu K, Zubair A, Liao AD, Fang W, Ouyang F, Lee YH, Ueno K, Saito R, Palacios T, Kong J, Dresselhaus MS. Large-Area Synthesis of High-Quality Uniform Few-Layer $MoTe_2$. J Am Chem Soc. 2015; 137:11892–11895. [PubMed: 26305492]
48. Kan M, Nam HG, Lee YH, Sun Q. Phase Stability and Raman Vibration of the Molybdenum Ditelluride ($MoTe_2$) Monolayer. Phys Chem Chem Phys. 2015; 17:14866–14871. [PubMed: 25982102]

49. Sun Y, Wang Y, Sun D, Carvalho BR, Read CG, Lee C-h, Lin Z, Fujisawa K, Robinson JA, Crespi VH, Terrones M, Schaak RE. Low-Temperature Solution Synthesis of Few-Layer 1T′-$MoTe_2$ Nanostructures Exhibiting Lattice Compression. Angew Chem Int Ed. 2016; 55:2830–2834.
50. Naylor CH, Parkin WM, Ping J, Gao Z, Zhou YR, Kim Y, Streller F, Carpick RW, Rappe AM, Drndic M, Kikkawa JM, Johnson ATC. Monolayer Single-Crystal 1T′-MoTe2 Grown by Chemical Vapor Deposition Exhibits a Weak Antilocalization Effect. Nano Lett. 2016; 16:4297. [PubMed: 27223343]
51. Hahn, T, editor. International Tables for Crystallography. 5. Springer; Dordrecht, The Netherlands: 2005. Vol. A: Space-Group Symmetry
52. Brown BE. The Crystal Structures of WTe_2 and High-Temperature $MoTe_2$. Acta Crystallogr. 1966; 20:268–274.
53. Boyd, RW. Nonlinear Optics. 3. Academic Press; San Diego, CA: 2008.
54. Kudryavtsev A, Lavrov S, Shestakova A, Kulyuk L, Mishina E. Second Harmonic Generation in Nanoscale Films of Transition Metal Dichalcogenide: Accounting for Multipath Interference. AIP Adv. 2016; 6:095306.
55. Clarke R, Marseglia E, Hughes H. A Low-Temperature Structural Phase Transition in β-$MoTe_2$. Philos Mag B. 1978; 38:121–126.
56. Song S, Keum DH, Cho S, Perello D, Kim Y, Lee YH. Room Temperature Semiconductor-Metal Transition of $MoTe_2$ Thin Films Engineered by Strain. Nano Lett. 2016; 16:188–193. [PubMed: 26713902]
57. Ribeiro HB, Pimenta MA, de Matos CJ, Moreira RL, Rodin AS, Zapata JD, de Souza EA, Castro Neto AH. Unusual Angular Dependence of the Raman Response in Black Phosphorus. ACS Nano. 2015; 9:4270–4276. [PubMed: 25752593]
58. Song Q, Pan X, Wang H, Zhang K, Tan Q, Li P, Wan Y, Wang Y, Xu X, Lin M, Wan X, Song F, Dai L. The In-Plane Anisotropy of WTe_2 Investigated by Angle-Dependent and Polarized Raman Spectroscopy. Sci Rep. 2016; 6:29254. [PubMed: 27404226]
59. Disclaimer: Certain commercial equipment, instruments, or materials are identified in this paper in order to specify the experimental procedure adequately. Such identification is not intended to imply recommendation or endorsement by the National Institute of Standards and Technology nor is it intended to imply that the materials or equipment identified are necessarily the best available for the purpose.
60. Erni, R. Aberration Corrected Imaging in Transmission Electron Microscopy. Imperial College Press; London: 2010.
61. Nemes-Incze P, Osváth Z, Kamarás K, Biró L. Anomalies in Thickness Measurements of Graphene and Few Layer Graphite Crystals by Tapping Mode Atomic Force Microscopy. Carbon. 2008; 46:1435–1442.
62. Kresse G, Hafner J. Ab Initio Molecular Dynamics for Liquid Metals. Phys Rev B: Condens Matter Mater Phys. 1993; 47:558.
63. Kresse G, Hafner J. Ab Initio Molecular-Dynamics Simulation of the Liquid-Metal-Amorphous-Semiconductor Transition in Germanium. Phys Rev B: Condens Matter Mater Phys. 1994; 49:14251.
64. Kresse G, Furthmüller J. Efficiency of Ab-Initio Total Energy Calculations for Metals and Semiconductors Using a Plane-Wave Basis Set. Comput Mater Sci. 1996; 6:15–50.
65. Kresse G, Furthmüller J. Efficient Iterative Schemes for Ab Initio Total-Energy Calculations Using a Plane-Wave Basis Set. Phys Rev B: Condens Matter Mater Phys. 1996; 54:11169.
66. Dion M, Rydberg H, Schröder E, Langreth DC, Lundqvist BI. Van der Waals Density Functional for General Geometries. Phys Rev Lett. 2004; 92:246401. [PubMed: 15245113]
67. Román-Pérez G, Soler JM. Efficient Implementation of a Van der Waals Density Functional: Application to Double-Wall Carbon Nanotubes. Phys Rev Lett. 2009; 103:096102. [PubMed: 19792809]
68. Klimeš, Jcv; Bowler, DR; MichaelidesVan der Waals, A. Density Functionals Applied to Solids. Phys Rev B: Condens Matter Mater Phys. 2011; 83:195131.
69. Togo A, Tanaka I. First Principles Phonon Calculations in Materials Science. Scr Mater. 2015; 108:1–5.

70. Aroyo MI, Kirov A, Capillas C, Perez-Mato J, Wondratschek H. Bilbao Crystallographic Server. II. Representations of Crystallographic Point Groups and Space Groups. Acta Crystallogr, Sect A: Found Crystallogr. 2006; 62:115–128.

71. Chen SY, Goldstein T, Venkataraman D, Ramasubramaniam A, Yan J. Activation of New Raman Modes by Inversion Symmetry Breaking in Type II Weyl Semimetal Candidate T′-$MoTe_2$. Nano Lett. 2016; 16:5852–5860. [PubMed: 27517466]

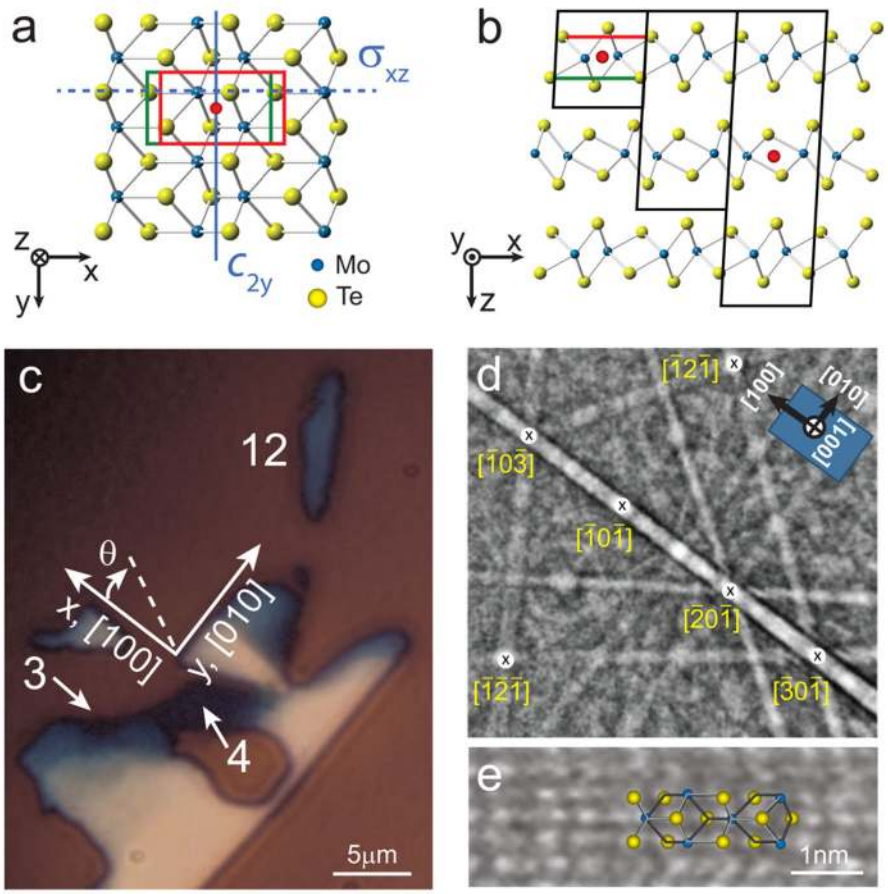

Figure 1.

(a) Top view of crystal structure of monolayer 1T′ $MoTe_2$. The green and red rectangles show two cuts of the unit cell parallel to the layer plane. The red dots indicate the center of inversion symmetry, the solid line indicates the $C_{2y}(0,1/2,0)$ screw axis, and the dashed line indicates the horizontal mirror plane σ_{xz}. (b) Side view of the crystal structure for monolayer ($N = 1$), bilayer ($N = 2$), and trilayer ($N = 3$) lattices. The red circles in the center of the $N = 1$ and 3 unit cells indicate inversion symmetry centers as well as $C_{2y}(0,1/2,0)$ screw axes perpendicular to the figure plane (along the y direction). The green and red lines are the projections of the respective rectangles in (a). (c) Light microscope image of $MoTe_2$ sample. The crystal orientation and regions with $N = 3$, 4, and 12 are indicated. The white dashed line indicates the polarization direction at an angle, θ, relative to the x-axis. (d) EBSD pattern from the flake in (a) with the Kikuchi lines indexed to the 1T′ crystal structure. Inset: The corresponding unit cell with the crystallographic directions labeled. (e) HAADF-STEM image of 1T′ $MoTe_2$. The intensity variations are attributed to the atomic number difference between Mo ($Z_{Mo} = 42$) and Te ($Z_{Te} = 52$).

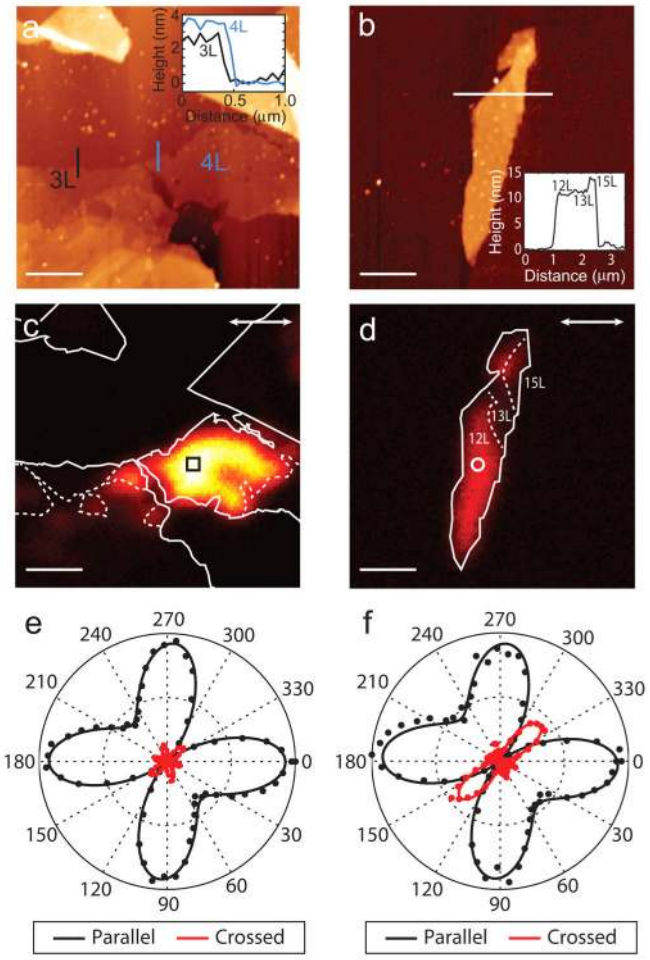

Figure 2.

(a) Topography of the $N = 3$ and 4 regions of the sample. Inset: Linecuts along the blue and black lines. (b) Topography of the $N = 12$ region. (c, d) SHG images of the regions shown in (a) and (b), respectively. The crystal and step edges are shown as solid and dashed lines, respectively. Color contrast is scaled by ×2 in (d). (e, f) SHG polar maps with the polarizer and analyzer parallel (black) and crossed (red) acquired at the black square ($N = 4$) in (c) white circle ($N = 12$) in (d), respectively. The angle is relative to the initial polarization (white double arrow in c and d) and in the direction defined in Figure 1c. Scale bar = 2 μm.

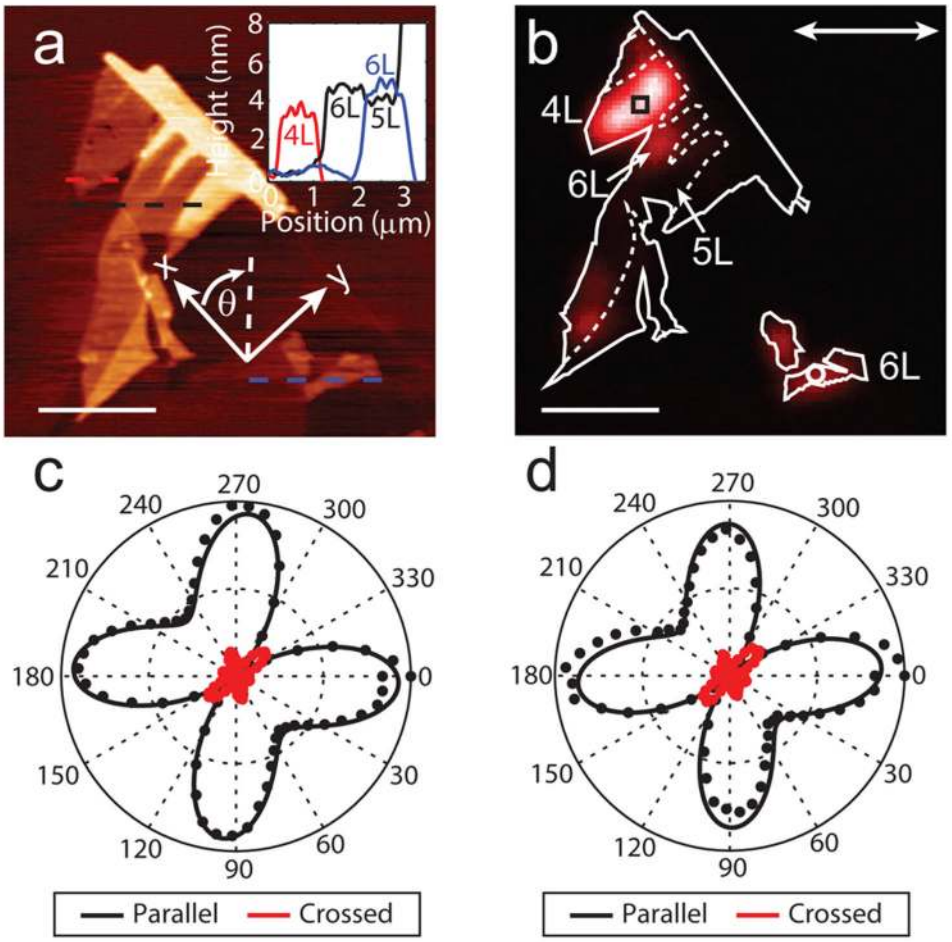

Figure 3.

(a) Topography and (b) SHG images of another sample. (c, d) SHG polarization polar maps with the polarizer and analyzer parallel (black) and crossed (red) acquired at the black square ($N = 4$) and white circle ($N = 6$) in (b), respectively. The crystallographic axes are shown in (a). The angle in the polar plots is relative to the initial polarization, shown as a white double arrow (b). Scale bar = 3 μm.

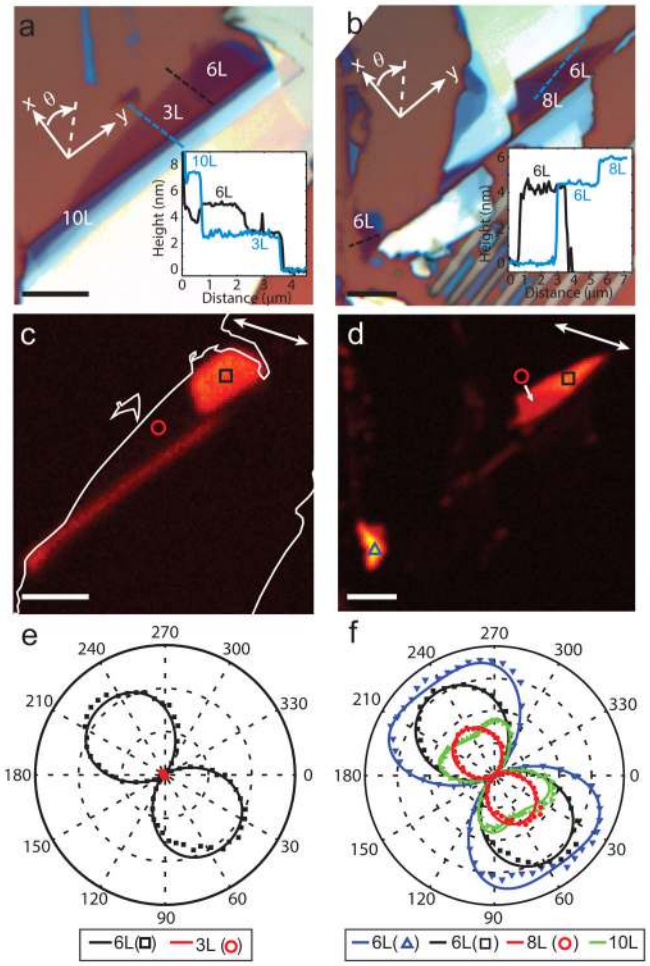

Figure 4.

(a, b) White light images with the layer thicknesses and crystallographic axes labeled. Insets: AFM profiles along the black and blue dashed lines. (c, d) SHG images with the excitation polarization direction shown as a white arrow. Color contrast is scaled by ×2 in (c) compared to (d). (e) SHG polarization polar map with the polarizer and analyzer parallel acquired at the black square ($N = 6$) and red circle ($N = 3$) in (c) are shown in black and red, respectively. (f) SHG polarization polar map with the polarizer and analyzer parallel acquired at the blue triangle ($N = 6$), the black square ($N = 6$), red circle ($N = 8$) in (d) and a nearby region ($N = 8$) are shown in blue, black, red, and green, respectively. The angle in the polar plots is relative to the horizontal axis in (b and c). Scale bar = 5 μm.

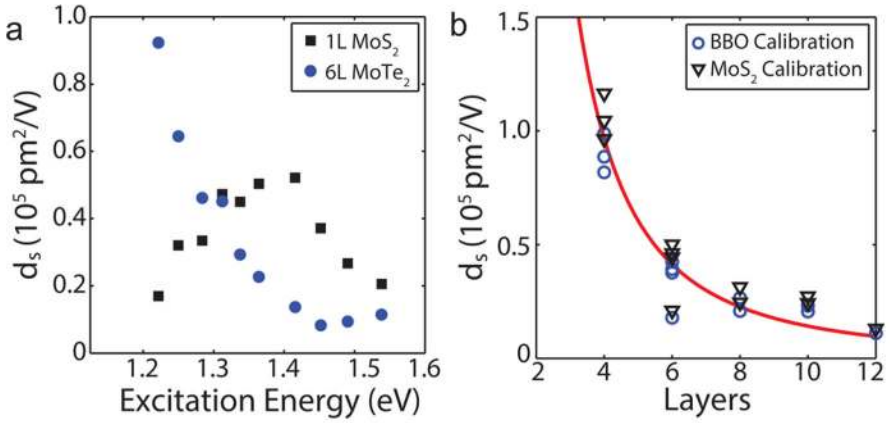

Figure 5.

(a) Wavelength-dependent d_s of 1T′ $MoTe_2$ (blue circles) and monolayer MoS_2 (black squares) calibrated using BBO. (b) Layer-dependent surface second-order susceptibility, d_s, of 1T′$MoTe_2$ calibrated using BBO (blue circles) and monolayer MoS_2 (black triangles). Solid line is empirically fit using $d_s(N) = 1.8x10^6\ N^{-2}$ pm^2/V.

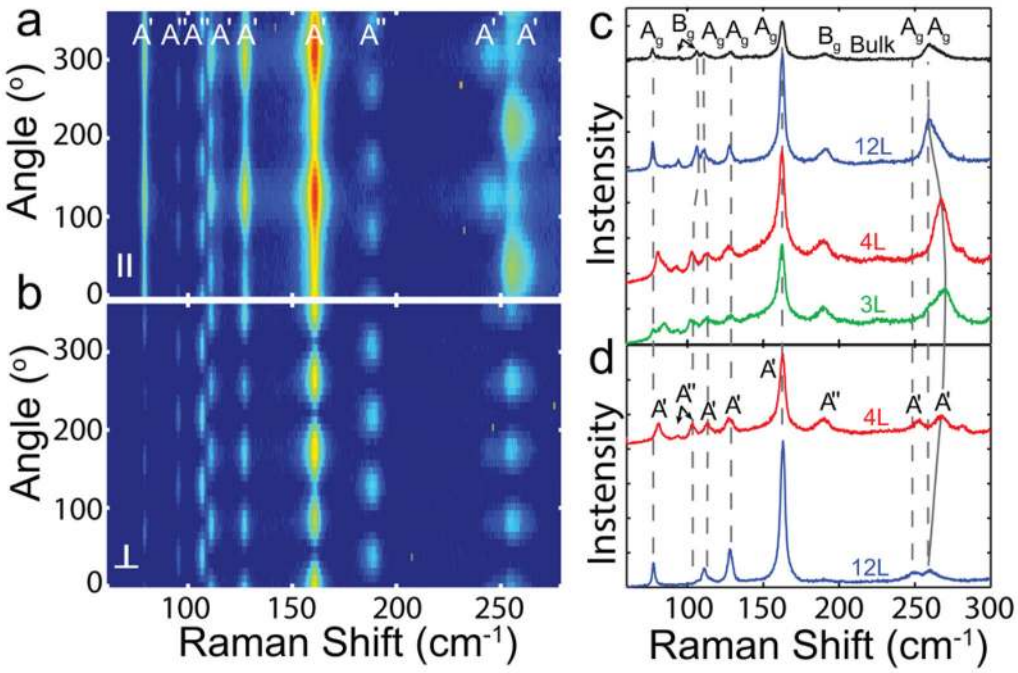

Figure 6.

(a, b) Raman polarization dependence with the polarizer and analyzer parallel and crossed for the $N = 12$ region on a logarithmic scale. The Raman modes are labeled according to the symmetry. (c) Unpolarized Raman spectra of the bulk (black), $N = 12$ (blue), and $N = 4$ regions (red). (d) Example spectra of the $N = 4$ and 12 regions in a parallel configuration show the doublet at ≈260 cm^{-1}.

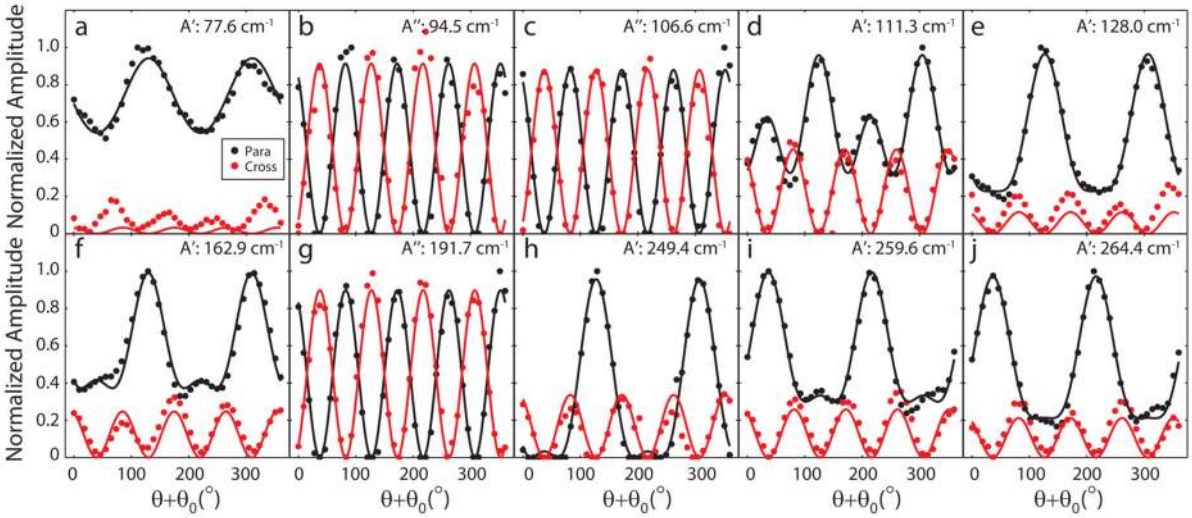

Figure 7.

Normalized Raman amplitudes for parallel (red) and crossed (black) polarizations for the $N = 12$ region. The solid lines are the fits using the complex Raman tensors. The symmetry and frequency for each mode are labeled. The fits give $\theta_0 = -53°$. Taking into account the difference in mounting angle between the SHG and Raman systems ($\approx -10°$), the crystal orientations from the Raman measurements are in excellent agreement with the SHG measurements.

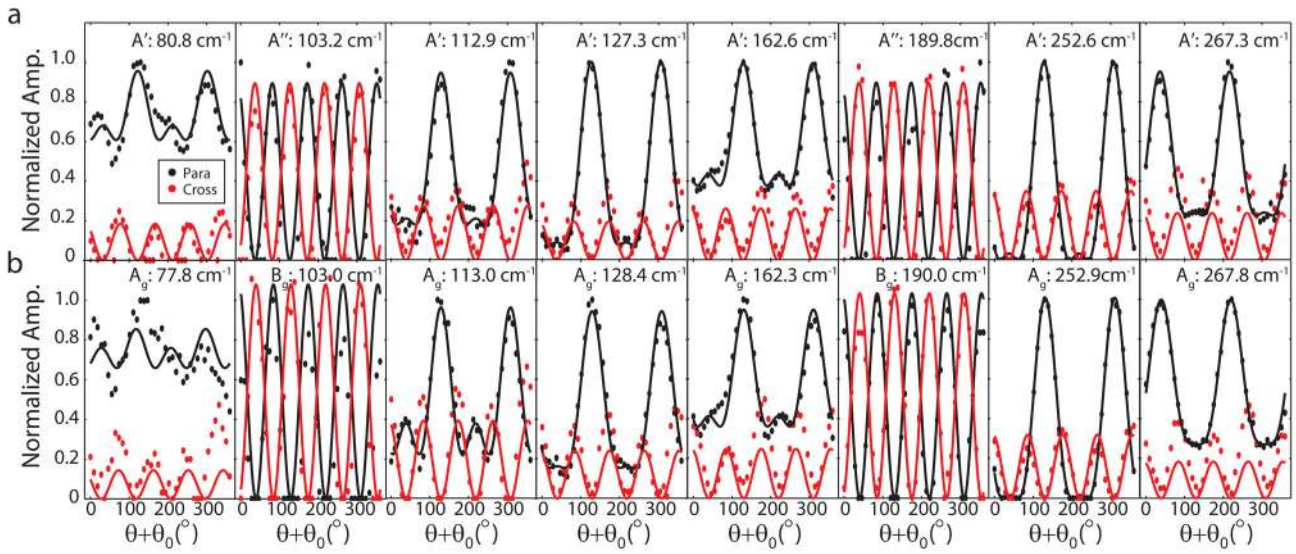

Figure 8.

Normalized Raman amplitudes for parallel (red) and crossed (black) polarizations for the (a) $N = 4$ and (b) $N = 3$ regions of the sample in Figure 1. The solid lines are the fits using the complex Raman tensors. The symmetry and frequency for each mode are labeled. The fits give $\theta_0 = -52.5°$. Taking into account the difference in mounting angle between the SHG and Raman systems ($\approx -10°$), the crystal orientations from the Raman measurements are in excellent agreement with the SHG measurements.

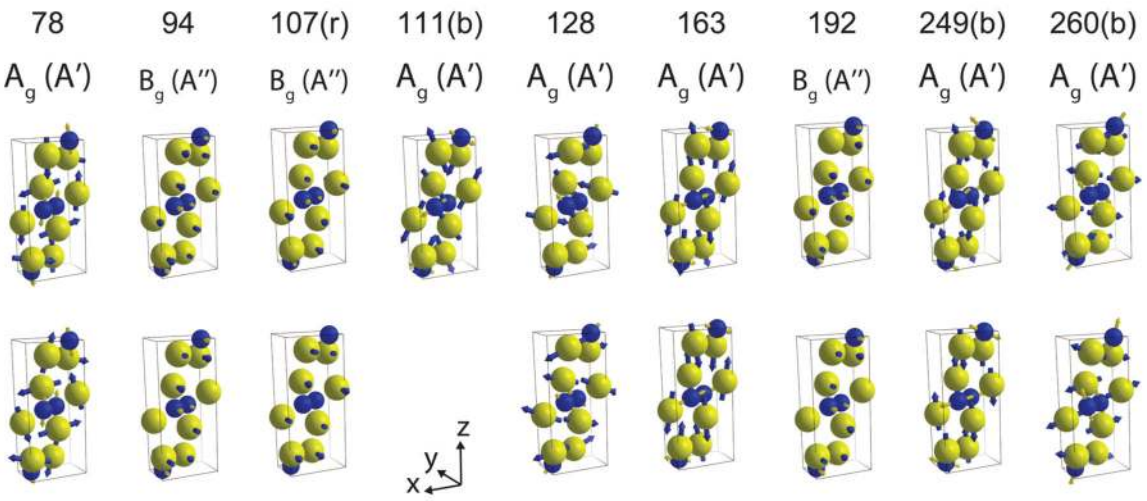

Figure 9.

Summary of the Raman modes in N-layer 1T′ $MoTe_2$ with N odd and N even. Modes that blue or red shift as the crystals get thinner are indicated with (b) and (r), respectively. Reported Raman shifts are for $N = 12$. Normal mode atomic displacements of bulk 1T′-$MoTe_2$ are shown as blue and yellow arrows for displacement of Te and Mo atoms, respectively. The magnitude of the displacements is proportional to the length of arrows. Blue and yellow spheres denote Mo and Te atoms, respectively. The primitive cells of bulk 1T′-$MoTe_2$ are shown by black boxes.

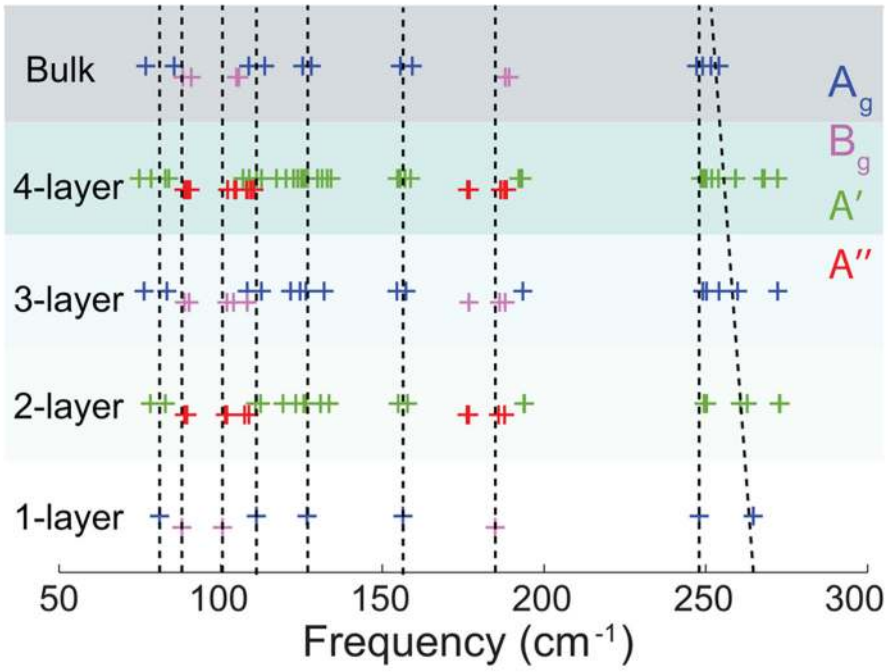

Figure 10.

Raman active modes of *N*-layer $MoTe_2$ are plotted. Blue, magenta, green, and red symbols denote A_g, B_g, A′, and A″ modes, respectively. The B_g and A″ are offset from the A_g and A′ modes for clarity. Dashed lines are drawn as guides for comparison of the peak frequencies between the five materials.

Table 1

Summary of Lattice Vibration Representations for N-Layer 1T′ $MoTe_2$ with N Odd and N Even

	N odd (C_{2h}^2)	N even(C_s^1)
Raman	$6N\,A_g \oplus 3N\,B_g$	$6N\,A' \oplus 3N\,A''$
infrared	$(3N-1)\,A_u \oplus (6N-2)\,B_u$	$(6N-2)\,A' \oplus (3N-1)\,A''$
acoustic	$A_u \oplus 2\,B_u$	$2\,A' \oplus A''$